Assembly of Tailored Porous Nanofibers from Mesoporous MCM-41 Nanoparticles via Electrospinning

Jana Timm, Michael Furtmair, and Roland Marschall*[a]

Abstract: For the first time the assembly of isolated and purified MCM-41 nanoparticles into nanofibers was realized by electrospinning. Electrospinning was conducted with a dispersion of these nanoparticles and polyvinylpyrrolidone in ethanol. The nanofibers were characterized by electron microscopy, X-ray diffraction, elemental analysis, gas physisorption and infrared spectroscopy in diffuse reflectance. The variation of the spinning parameters was investigated in detail towards the influence on the nanofiber diameter. The change of the applied voltage and the flow rate show strong impacts on the nanofiber diameter. Therefore, the nanofiber diameter can be tailored by choosing suitable electrospinning parameters. The fiber mats with thin nanofibers were then additionally functionalized with sulfonic acid groups in a proof of principal study. The nanofiber morphology was maintained both after functionalization with thiol group and subsequent oxidation to sulfonic acid groups.

Introduction

The possibility to synthesize highly ordered mesoporous silica (OMS) materials, which were named after the Mobil Oil Company, Mobil Composition of Matter (MCM), was discovered in 1992.[1,2] In this new class of materials the tailoring of highly ordered mesopores is possible, so the pores can be arranged in 3D cubic (MCM-48), 2D hexagonal (MCM-41) or even lamellar pore structure (MCM-50).[3,4] MCM materials are synthesized in template-based sol-gel processes, where the template and the reaction parameters define the pore size and the pore structure. The removal of the organic template is done by (Soxhlet) extraction or calcination.[5] After removal of the template the MCM material class offers highly ordered mesopores, which allow e.g. the formation of nanoreactors in the pores.[6–8] Further due to mesoporosity (pore sizes between 2 to 50 nm), MCM materials provide very high surface area (up to 1500 $m^2 g^{-1}$), which is very promising for different fields of application like catalysis,[9–14] medicine,[15–20] proton conduction[21–27] or purification/adsorption processes[28–32] and immobilization processes,[33–36] like e.g. immobilization of catalysts.[37–40] Another very attractive characteristic of MCM materials is the fact that these materials consist only of silica (SiO_2), which is non-toxic for our body, so the application in and on our body is possible.[41–43] Therefore, MCM materials are also perfect platforms for biomedical applications.[44,45] However, the material and biological interactions should not be neglected,

especially in case of nanomaterials.[46,47] Regarding the MCM materials another huge advantage is the option to tailor these materials *via* different techniques. Tailoring the morphology of MCM materials is possible regarding e.g. particle size.[48–50] A new possibility to assemble MCM-41 materials is presented in the following.

Electrospinning can be used to prepare polymeric fiber mats with macroporous voids.[51] It is a widely used technique to produce polymer, carbon, or oxide fibers for different applications.[52–55] In general, a solution or a melt is filled in a syringe and pressed out of a metal needle with constant speed using a syringe pump, while a high voltage is applied between the needle tip and a collector. When enough voltage is applied, the surface tension of the solution/dispersion droplet at the needle tip breaks down and a jet of the solution erupts. This effect leads to the formation of multilayer fiber mats at the collector, which can be removed and are ready for further treatments. The diameter of the resulting fibers is in the nanosize regime depending on the material and electrospinning parameters. Thus, the fiber mat forms macroporous voids (pore sizes >50 nm[56]) due to overlaying nanosized fibers. Therefore, the advantage of the electrospinning procedure is that the fiber mats are very light due to macroporosity, but exhibit also a lot of active material. Additionally, the possibility to prepare a lot of material *via* electrospinning in short times is available.[55,57]

The electrospinning procedure is very often based on sol-gel processes[55,58–62] or polymerization,[63–65] while electrospinning of particle dispersion is possible but only rarely used.[64,66] To the best of our knowledge, here for the first time the electrospinning procedure was used to prepare mesoporous nanofibers which only consist of pre-synthesized, isolated and purified MCM-41 nanoparticles. Combining the synthesis of nanosized pre-synthesized MCM-41 particles with the process of electrospinning enables both macroporosity and multiple mesoporosity in one material, leading to hierarchically porous fiber mats. We also present the assembly of ordered mesopo-

[a] Dr. J. Timm, M. Furtmair, Prof. Dr. R. Marschall
Department of Chemistry
University of Bayreuth
Universitätsstrasse 30, 95447 Bayreuth (Germany)
E-mail: roland.marschall@uni-bayreuth.de

rous MCM-41 nanoparticles into nanofibers while adjusting the nanofiber diameter by variation of the electrospinning parameters. Additionally, we functionalize the fiber mats to push the feasibility of the preparation of MCM-41 particle-based nanofibers and the subsequent functionalization to the next level towards application with tailor-made materials. Most importantly, the nanofibers morphology is retained throughout the whole functionalization process.

Results and Discussion

As standard electrospinning parameters 12 kV voltage, a dispersion of 5 wt.% MCM-41 nanoparticle in a solution containing 10 wt.% polyvinylpyrrolidone (PVP) in ethanol, a needle tip diameter of 0.8 mm, and a flow rate of 0.9 mL/h were chosen. After the electrospinning process the nanofiber mats were taken off the collector. To understand the formation of the nanofibers as interaction between the spinning polymer PVP and the pre-synthesized MCM-41 nanoparticles, TEM images were taken of the nanofibers directly after the spinning process (Figure 1). In the TEM images the MCM-41 nanoparticles are presented as darker spots, while the PVP is brighter. The MCM-41 nanoparticles are nicely distributed along the whole fiber. In some parts, a higher accumulation of the particles can be seen leading to thicker nanofiber diameters.

To get the advantage of the mesoporosity of the MCM-41 nanoparticles back, the whole fiber mat was calcined at 200 °C for 16 h and at 500 °C for 6 h to remove all organic residuals like e.g. the spinning polymer and solvent molecules. After that treatment the MCM-41 nanoparticle-based nanofiber (NF) is finally manufactured.

After heat treatment the NF morphology, which was already observed in the TEM images (Figure 1), is retained. The SEM images show a fiber diameter of 416 nm ($\pm$119 nm) (averaged value) (Figure 2). The voids between the NFs are bigger than 100 nm and therefore macroporous. The MCM-41 nanoparticles are nicely visible and showing the assembly of particles to form NFs. In some parts the NFs are thicker in diameter compared to other fibers which is in good agreement to TEM results.

The removal of the organic residuals was investigated by diffuse reflectance infrared Fourier transformation spectroscopy (DRIFTS).

In the DRIFT spectrum of the thermally-treated MCM-41 NF all arising vibrations could be assigned to either as Si–O or Si–OH vibrations in SiO_2 (Figure 3, left).[67–69] No band belonging to polymer residues can be observed. Si–O vibrations cause the absorption bands at 1987 and 1865 cm^{-1}.[67,70] Further the relatively broad signal at 3420 cm^{-1} and the absorption band at 1630 cm^{-1} originate from adsorbed water on the silica surface.[67,71] The sharp absorption band at 3743 cm^{-1} indicates the presence of isolated silanol groups on the surface.[68,72,73] The XRD pattern of the thermally-treated MCM-41 NFs shows three intense reflections at 2.5, 4.1 and 4.8 °2θ. The presence of these three reflections confirms that the 2D hexagonal ordered pore structure of the nanoparticles is preserved during the electrospinning process. Compared to literature the °2θ values are slightly higher.[21] Further it shows that the lattice constant a_0 is slightly larger and that the pore size is therefore increased compared to literature.[21] Furthermore the nitrogen physisorption isotherm of the thermally-treated MCM-41 NF shows clearly the mesoporosity of the MCM-41 nanoparticles. The specific surface area is 1163 m^{2}g^{-1}, while the pore size is 3.5 nm (Figure 4). Compared to literature the pore size is slightly bigger, as already expected from XRD data of the NFs, and the specific surface area is also slightly lower due to the slightly bigger pores in the NFs.[21]
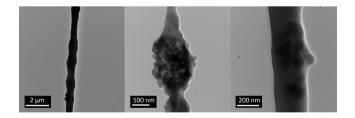

Figure 1. TEM images of the electrospun nanofibers based on MCM-41 nanoparticles with standard electrospinning parameters directly after electrospinning process (before polymer removal).
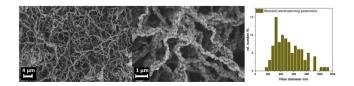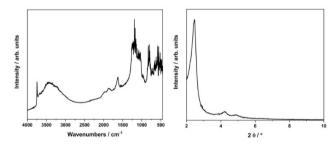

Figure 2. SEM image of the electrospun NF based on MCM-41 nanoparticles with standard electrospinning parameters after removal of organic residuals and the resulting fiber diameter distribution.

Figure 3. DRIFT spectrum (left) and XRD pattern (right) of the MCM-41 NF after removal of organic residuals.
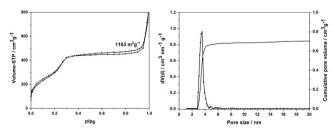

Figure 4. Nitrogen physisorption data of the MCM-41 NF after removal of organic residuals (left) and the corresponding pore size distribution (right).

In the electrospinning process, the interplay between the spinning parameters (applied voltage between needle tip and collector, needle tip diameter and flow rate through the syringe) is essential to investigate in order to be able to tailor the fiber diameter.

At first, we varied the needle tip diameter. In Figure 5a the variation of the needle tip diameter is presented in comparison to the fiber diameter distribution of NF achieved with standard electrospinning parameters (needle tip diameter: 0.8 mm; flow rate: 0.9 mL/h, applied voltage: 12 kV same dispersion as always). The fiber diameter was determined from SEM images in Figure S1. The impact on the diameter of the needle tip is negligible and no clear trend is visible, only very slight changes are visible compared to NFs prepared with standard electrospinning parameters. The needle tip diameter of 0.6 mm leads to an averaged NF diameter of around 505 nm ($\pm$178 nm), while 0.8 mm (standard parameters) and 0.9 mm needle tip diameters lead to an averaged NF diameter of around 416 nm ($\pm$119 nm) and 460 ($\pm$134 nm) nm, respectively.

Further, we varied the flow rate through the syringe, while all other spinning parameter (needle tip diameter, applied voltage, same dispersion as always) remaining as standard. After evaluation of SEM images (Figure S2) the dependence on the flow rate is presented in Figure 5b. The fiber diameter increases with increasing flow rates. Thus, with a flow rate of 0.3 mL per hour (mL/h) NFs with an averaged diameter of 252 nm ($\pm$81 nm) were achieved, while with a flow rate of 0.5 mL/h, 0.7 mL/h and 0.9 mL/h (standard parameters) an averaged diameter of 280 nm ($\pm$105 nm), 405 nm ($\pm$130 nm) and 416 nm ($\pm$119 nm) could be prepared. The effect of increasing NF diameter with increasing flow rate was also observed in literature for polymer nanofibers, where the terminal diameter of the jet (also proportional to the NF diameter) is proportional to the flow rate.[64,74] Interestingly, the dispersion of MCM-41 nanoparticles used here shows comparable behavior to polymer solutions in the electrospinning procedure, and opens up the possibility for tailoring the NF diameter.

Another important electrospinning parameter is the electric current/applied voltage between the needle tip and the collector.[64,74] In Figure 6a–e the variation in the applied voltage compared to the standard electrospinning parameters is presented. The NF diameter distribution is taken from the SEM images in Figure S3/S4. With increasing applied voltage, the NF diameter is decreasing. Therefore, the thinnest NFs (averaged diameter 242 nm ($\pm$98 nm)) were obtained at an applied
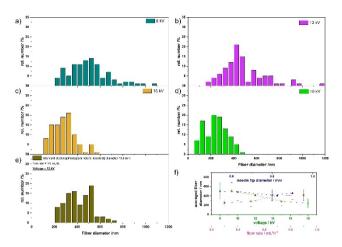

Figure 6. Relative distribution of fiber diameter depending on the applied voltage between the needle tip and the collector.

voltage of 18 kV, while with 8 kV, 10 kV, 12 kV (standard parameters) and 15 kV averaged diameter of 500 nm ($\pm$174 nm), 478 nm ($\pm$181 nm), 416 nm ($\pm$119 nm) and 284 nm ($\pm$101 nm) were obtained, respectively. Also this dependency of the applied voltage and the NF diameter is known for polymer NFs in an inverse correlation, as it is also observed here.[64,74] This finding further underlines that the used dispersion is comparable to polymer solutions in the electrospinning process, and makes it therefore easy to adjust the NF diameter and to tailor these NFs for different applications.

In Figure 6f the dependence of all varied parameters and the NF diameter are presented. Due to this detailed studies, it is possible to choose the desired NF diameter only by setting the experimental conditions.

To approach the minimum NF diameter, NFs with an applied voltage of 18 kV and a flow rate of 0.3 mL/h were produced. With these conditions NFs with an averaged diameter of 253 nm ($\pm$84 nm) and narrow NF diameter distribution could be obtained (Figure 7). Thus, it seems that the minimum in NF diameter is reached around 250 nm as averaged NF diameter. In TEM images (Figure S5) the ordered mesoporous pore structure and the assembly of the MCM-41
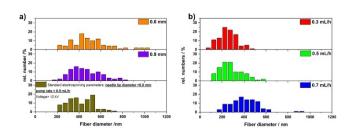

Figure 5. Relative distribution of fiber diameter depending on the needle tip diameter (a) and depending on the flow rate (b).
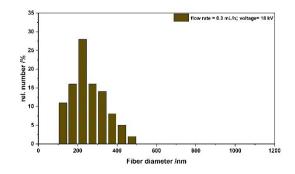

Figure 7. Relative distribution of fiber diameter for NFs prepared with an applied voltage of 18 kV and a flow rate of 0.3 mL/h.

nanoparticles into thin NFs is also visible. It is very obvious here that only a few NPs are assembled at the thickest points of the NF. This further underlines that the minimum in NF thickness of around 250 nm is already reached, which is possible by applying 18 kV during electrospinning process regardless of the flow rate.

To push the NFs further towards possible application and tailoring options, the functionalization of the MCM-41 NFs with organic functional groups is very important. Moreover, to keep the advantages of hierarchical porosity, a retainment of the nanofiber morphology is necessary. For the functionalization, we decided to incorporate/immobilize sulfonic acid (−SO$_3$H) groups on the MCM-41 surface. Sulfonic acid groups are present

in a lot of functional materials due to several reasons. Solid materials with immobilized sulfonic acid groups are used in heterogeneous catalysis,[75–82] as adsorbents,[83] as well as solid state proton conductors[21,84–86]

For the functionalization with sulfonic acid groups, a stepwise process was used. First 3-mercaptopropyl–trimethoxysilane (MPTMS) is grafted onto the surface *via* a solvent free procedure, which was developed in our working group.[87] Afterwards, the terminal thiol groups are oxidized by hydrogen peroxide solution. Here, the fiber mat with thinnest NFs was chosen (standard electrospinning parameters except of flow rate and applied voltage: 0.3 mL/h and 18 kV).

The SEM images (Figure 8) and the resulting fiber diameter analysis of the functionalized NFs (Figure 9) shows that the fiber diameter slightly increases from an averaged diameter of 253 nm (±84 nm, non-functionalized) to 343 nm (±122 nm, thiol functionalized) and finally to 368 nm (±114 nm, sulfonic acid functionalized). The increase in NF diameters could be explained with the functionalization also on the outer surface of the NFs. Therefore, the increase in NF diameter is more pronounced between the non-functionalized and the thiol functionalized NFs. After functionalization of the NFs the fiber morphology is preserved. This is outstanding and very unique, and can be explained with the mild reaction conditions of the chemical vapor deposition (CVD) functionalization routine.[87] The functionalization hardly leads to any fractures in NFs induced by the shaking procedure during the oxidation (SEM images on the left of Figure 8).

To investigate the changes of the inner surface of the mesoporous nanoparticle-based NFs, nitrogen physisorption measurements were conducted. In Figure 10 the nitrogen physisorption isotherms and the resulting pore size distributions (PSD) of the functionalized NFs in comparison to the non-functionalized NFs are presented. The specific surface area of the NFs (0.3 mL/h flow rate and 18 kV during electrospinning) exhibits almost the same value compared to the NFs which were electrospun with 12 kV (standard conditions) and also with the literature known particles.[21] This illustrates clearly that during electrospinning, no change in the particle morphology happens even if the applied voltage and flow rate is changed. Further, the pore size of 3.3 nm is comparable with the standard NFs (see Figure 3, 3.5 nm) and also with literature.[21]
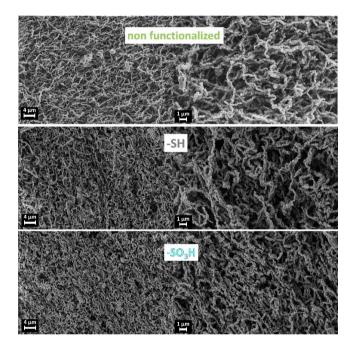

Figure 8. SEM images of the NFs after functionalization of the MCM-41 NP NFs via CVD method to achieve terminal thiol groups on the surface and subsequent oxidation with hydrogen peroxide to transfer thiol groups into sulfonic acid groups.
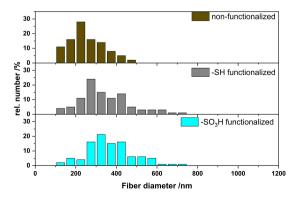

Figure 9. Fiber diameter of the NFs after functionalization of the MCM-41 NP NFs via CVD like method to achieve terminal thiol groups on the surface and subsequent oxidation with hydrogen peroxide to transfer thiol groups into sulfonic acid groups.
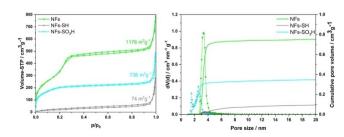

Figure 10. Nitrogen physisorption isotherms and resulting pore size distributions for the non-functionalized, thiol-functionalized and sulfonic acid functionalized NFs.

During the CVD-like functionalization the MPTMS gets into the pores. The pores are almost completely filled after that functionalization step. This effect is clearly visible in the pore size distribution (PSD) of the NFs—SH due to absence of accessible pores, which was already observed for other ordered mesoporous materials.[87] After the CVD functionalization the thiol groups were oxidized with hydrogen peroxide and the mesopores with a size of 2.6 nm in the NFs are recovered. The shrinkage of the mesopores from non-functionalized NFs to sulfonic acid functionalized NFs is due to the incorporation of the propyl chain with sulfonic acid as head group and was already observed for other ordered mesoporous silica materials.[87]

The successful functionalization could be further confirmed by DRIFTS (Figure 11). The present vibrations in the spectrum of the non-functionalized sample are comparable with the standard sample (Figure 3) and could be assigned to different Si—O and Si—OH vibrations.[67–71,73] In case of the thiol-functionalized sample the additional signals between 3020 to 2790 cm^{-1} could be assigned to vibrations of the alkyl chain in the MPTMS, while the signal at 2566 cm^{-1} arises from the vibration of the thiol group in MPTMS.[87–90] After CVD like functionalization of the NFs the absorption band of the isolated silanol groups disappears, which indicates that all suitable silanol groups on the surface have reacted with MPTMS to form covalent bounds. The highest possible functionalization density is therefore achievable, as it was already observed for other mesoporous materials before.[87] The oxidation of the thiol groups was done by aqueous hydrogen peroxide solution, and the change in the absorption band of the thiol group (at 2566 cm^{-1}) is obvious. The oxidation of the thiol groups is successful and quantitative, which is indicated in the absence of the thiol group vibration after reaction with aqueous hydrogen peroxide solution. Furthermore, the vibration signal of the isolated silanol groups (3743 cm^{-1}) remains absent, which shows that the oxidation does not damage the covalent linkage between the silica surface and the oxidized MPTMS linker. It can also be observed that during oxidation excess MPTMS molecules are being removed due to less intense vibrations of the alkyl chain of the oxidized MPTMS linker molecules, which can be explained by non-surface bound MPTMS from the earlier step.

The XRD pattern of the NFs (Figure 11) shows three reflections at 2.5, 4.1 and 4.8 °2θ. These values are comparable with the NFs with the standard procedure and also with
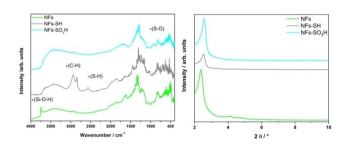
literature values.[21] During functionalization the 2D hexagonal structure of the pores remains, even though the reflections at 4.1 and 4.8 °2θ disappear. This disappearance can be explained with the functionalization and the filling of the pores with organic linker molecules.[87]

The successful functionalization and subsequent oxidation could be further confirmed by elemental analysis (EA) and the determination of the ion exchange capacity (IEC) via titration of the sulfonic acid containing NFs. The EA results indicate a sulfur content of 7.9% in NFs—SH (2.46 mmol g^{-1}) and 4.0% in NFs—SO_3H (1.25 mmol g^{-1}). For the sulfonic acid containing sample it is also possible to determine the ion exchange capacity (IEC) via acid-base titration. For NFs—SO_3H the IEC is 1.44 mmol g^{-1}. The IEC is comparable with the results from EA. This underlines that every sulfur atom in NFs—SO_3H was converted into sulfonic acid group, and the oxidation of the thiol groups towards sulfonic acid groups was quantitative.

Conclusions

For the first time we showed the possibility to assemble isolated and purified MCM-41 nanoparticles *via* electrospinning into porous nanofibers. We found that the ordered mesoporosity of the MCM-41 nanoparticles is retained in the resulting nanofibers. Furthermore, spinning parameters like applied voltage and flow rate play an important role in tailoring the nanofiber diameters, while the influence of the needle tip diameter can be neglected. The prepared nanofibers can be tailored in diameter between 250 nm and 500 nm. Additionally, we successfully functionalized the hierarchically mesoporous nanofiber mats with sulfonic acid groups by a very mild reaction route. Most importantly, the nanofibers morphology is retained both during this CVD-like grafting process with propyl—thiol chains and the oxidation to sulfonic acid groups. This procedure can pave the way towards new types of nanostructured inorganic proton-conducting membranes in the future.

Experimental Section

Synthesis of MCM-41 nanoparticles

In a typical synthesis[21] 0.7 mL of NaOH solution (2 M, Merck) and 96 mL of water were mixed and heated upon 80 °C. Then 0.2 g of the surfactant cetyltrimethylammonium bromide (CTAB, Sigma-Aldrich) were added and dissolved. Subsequent 1 mL of Tetraethylorthosilicate (TEOS, VWR Chemicals) was added to the solution. After stirring for 2 h at 80 °C the mixture was cooled down in an ice bath, centrifuged at 8000 rpm for 10 minutes and washing with water and ethanol. The white powder was dried at 80 °C overnight.

Preparation of electrospun MCM-41 fiber mats

5 wt-% MCM-41 NP and 10 wt-% polyvinylpyrrolidone (PVP, MW = 1.3 MDa, Alfa Aesar) were dispersed in ethanol (VWR Chemicals) by using ultrasonication. After reaching well-dispersed MCM-41 NPs the dispersion was transferred to a syringe and placed in a syringe pump for the electrospinning process in an electrospinning

Figure 11. DRIFT spectrum (left) and XRD pattern (right) of the functionalized thin NFs.

chamber. 40% of rel. humidity were set in the chamber, the distance between the needle tip and the rotating drum collector was fixed to 15 cm. The standard spinning parameter were then a needle tip diameter of 0.8 mm, a flow rate through the syringe of 0.9 mL/h and applied voltage of $+12$ kV. The fiber mats were removed from the collector and heat treated at 200 °C for 16 h and 500 °C for 6 h (heating rate: 1 K/min) to obtain the template- and polymer-free NFs mats.

Functionalization of the NF mat

In a general synthesis, 0.08 g of NF mat was put in a tiny beaker inside a Teflon inlet of a stainless-steel autoclave, then 1 mL MPTMS (3-mercaptopropyl–trimethoxysilane, Sigma-Aldrich) was filled in another tiny beaker inside the Teflon inlet. The Teflon inlet was flushed with argon for 1 min. The vessel was transferred to the autoclave and sealed. After sealing the autoclave was heated in an oven for 48 h at 120 °C. After cooling the white NF mat was carefully taken out of the Teflon inlet of the autoclave, was washed very carefully with water and dried in air (T = 25 °C, 72 h). The subsequent oxidation of MPTMS-functionalized NFs was conducted by shaking the NF mat in a mixture of 13 mL conc. H_2O_2 solution and 1.5 mL conc. HNO_3 for 24 h at room temperature. Afterwards, the NF mat was carefully removed from the solution, washed several times with water and ethanol, and dried in air (T = 25 °C, 72 h).

Characterization

SEM images were recorded with a Zeiss LEO 1530. An acceleration voltage of 3 kV was applied with an aperture set to 30 μm. Prior to the measurement all samples were sputtered with 1 to 2 nm Pt using a Cressington Sputter Coater 208 HR. TEM images were recorded with a JEOL JEM-2200FS EFTEM equipped with Schottky FEG and In-Column Omega Energy filter from JEOL operated at 200 kV. As TEM sample preparation 1 to 2 mg of the sample were suspended in 1 mL of ethanol (AcrosOrganics, extra dry, 99.5%) and afterwards 4 μL of the suspension was dropped on a carbon film coated Cu TEM grid (200 Mesh). SEM and TEM images were processed using ImageJ. X-ray diffraction (XRD) patterns were measured with a Malvern PANalytical Empyrean diffractometer using Cu Kα irradiation. Acceleration voltage and emission current were set to 40 kV and 40 mA, respectively. Nitrogen physisorption measurements were conducted at −196.15 °C with an Anton Paar QUADRASORB evo surface area & pore size analyzer. The samples were degassed for 16 hours at 120 °C in vacuum prior to the measurement. The data analysis was done via software ASiQwin™ (Anton Paar QuantaTec, Boynton Beach, USA). For titration 10 mg of sulfonated NF mats were stirred in 100 mL 0.001 M sodium hydroxide solution for 24 h at room temperature, then centrifuged, filtrated and the liquid decanted. The solution was titrated against 0.001 M hydrochloric acid solution with a Titroline 7000 (SI Analytics) to pH 7. For elemental analysis (C, H, N, S) precise quantities of samples between 2–3 mg were placed in a tin boat and sealed. The sealed package was placed in a Unicube from Elementar. During the measurement the combustion tube was heated up to 1143 °C in O_2/Ar atmosphere to ensure a complete combustion of the samples. The detection of completely oxidized gaseous species was done *via* thermal conductivity system. Diffuse reflectance infrared Fourier transform (DRIFT) spectra were collected using a Bruker alpha II with exchangeable sample attachments.

Conflict of Interests

The authors declare no conflict of interest.

Data Availability Statement

The data that support the findings of this study are available on request from the corresponding author. The data are not publicly available due to privacy or ethical restrictions.

[1] C. T. Kresge, M. E. Leonowicz, W. J. Roth, J. C. Vartuli, J. S. Beck, *Nature* **1992**, *359*, 710–712.
[2] J. S. Beck, J. C. Vartuli, W. J. Roth, M. E. Leonowicz, C. T. Kresge, K. D. Schmitt, C. T. W. Chu, D. H. Olson, E. W. Sheppard, S. B. McCullen, J. B. Higgins, J. L. Schlenker, *J. Am. Chem. Soc.* **1992**, *114*, 10834–10843.
[3] F. Hoffmann, M. Cornelius, J. Morell, M. Fröba, *Angew. Chem. Int. Ed.* **2006**, *45*, 3216–3251.
[4] I. Díaz, J. Pérez-Pariente, O. Terasaki, *J. Mater. Chem.* **2004**, *14*, 48–53.
[5] F. Hoffmann, M. Fröba, *Chem. Soc. Rev.* **2011**, *40*, 608–620.
[6] Y. Ma, H. Zhang, R. Lin, Y. Ai, K. Lan, L. Duan, W. Chen, X. Duan, B. Ma, C. Wang, X. Li, D. Zhao, *Nat. Commun.* **2022**, *13*, 6136.
[7] J. Zhao, R. Jian, Y. Wang, B. Yang, D. Zhao, C. Shen, L. Qiao, B. Liu, *ACS Appl. Mater. Interfaces* **2021**, *13*, 11571–11578.
[8] M. Liong, S. Angelos, E. Choi, K. Patel, J. F. Stoddart, J. I. Zink, *J. Mater. Chem.* **2009**, *19*, 6251–6257.
[9] B. Rác, Á. Molnár, P. Forgo, M. Mohai, I. Bertóti, *J. Mol. Catal. A* **2006**, *244*, 46–57.
[10] A. L. De Lima, A. Mbengue, R. A. S. San Gil, C. M. Ronconi, C. J. A. Mota, *Catal. Today* **2014**, *226*, 210–216.
[11] K. K. Sharma, R. P. Buckley, T. Asefa, *Langmuir* **2008**, *24*, 14306–14320.
[12] F. Habeche, M. Hachemaoui, A. Mokhtar, K. Chikh, F. Benali, A. Mekki, F. Zaoui, Z. Cherifi, B. Boukoussa, *J. Inorg. Organomet. Polym. Mater.* **2020**, *30*, 4245–4268.
[13] S. Pasricha, P. Gahlot, K. Mittal, D. Rai, N. Avasthi, H. Kaur, S. Rai, *ChemistrySelect* **2022**, *7*, e202103674.
[14] Y. Zhao, Z. Wang, W. Yang, S. Gu, X. Yang, A. Kheradmand, X. Zhang, Y. Luo, J. Huang, Y. Jiang, *ChemNanoMat* **2021**, *7*, 927–934.
[15] M. Vallet-Regi, A. Rámila, R. P. Del Real, J. Pérez-Pariente, *Chem. Mater.* **2001**, *13*, 308–311.
[16] G. Sun, Y. Chang, S. Li, Q. Li, R. Xu, J. Gu, E. Wang, *Dalt. Trans.* **2009**, 4481–4487.
[17] C. Argyo, V. Weiss, C. Bräuchle, T. Bein, *Chem. Mater.* **2014**, *26*, 435–451.
[18] J. Galhano, G. A. Marcelo, M. P. Duarte, E. Oliveira, *Bioorg. Chem.* **2022**, *118*, 105470.
[19] M. Deaconu, I. Nicu, R. Tincu, A. M. Brezoiu, R. A. Mitran, E. Vasile, C. Matei, D. Berger, *Chem. Pap.* **2018**, *72*, 1869–1880.
[20] M. Jahns, D. P. Warwas, M. R. Krey, K. Nolte, S. König, M. Fröba, P. Behrens, *J. Mater. Chem. B* **2020**, *8*, 776–786.

[21] R. Marschall, I. Bannat, A. Feldhoff, L. Wang, G. Q. Lu, M. Wark, *Small* **2009**, *5*, 854–859.

[22] R. Marschall, C. Klaysom, A. Mukherji, M. Wark, G. Q. Lu, L. Wang, *Int. J. Hydrogen Energy* **2012**, *37*, 4012–4017.

[23] M. Furtmair, J. Timm, R. Marschall, *Microporous Mesoporous Mater.* **2021**, *312*, 110745.

[24] M. Sharifi, M. Wark, D. Freude, J. Haase, *Microporous Mesoporous Mater.* **2012**, *156*, 80–89.

[25] C. A. Alabi, M. E. Davis, *Chem. Mater.* **2006**, *18*, 5634–5636.

[26] J. C. Mc Keen, Y. S. Yan, M. E. Davis, *Chem. Mater.* **2008**, *20*, 5122–5124.

[27] N. Dvoyashkina, C. F. Seidler, M. Wark, D. Freude, J. Haase, *Microporous Mesoporous Mater.* **2018**, *255*, 140–147.

[28] Y. Belmabkhout, R. Serna-guerrero, A. Sayari, *Adsorpt. J. Int. Adsorpt. Soc.* **2010**, *49*, 359–365.

[29] Y. Belmabkhout, N. Heymans, G. De Weireld, A. Sayari, *Energy Fuels* **2011**, *25*, 1310–1315.

[30] Y. Belmabkhout, R. Serna-Guerrero, A. Sayari, *Adsorption* **2011**, *17*, 395–401.

[31] F. Suhail, M. Batool, M. I. Din, M. A. Khan, G. A. Chotana, I. Zubair, A. T. Shah, *J. Porous Mater.* **2020**, *27*, 1491–1504.

[32] Y. Bao, X. Yan, W. Du, X. Xie, Z. Pan, J. Zhou, L. Li, *Chem. Eng. J.* **2015**, *281*, 460–467.

[33] Y. Wang, F. Caruso, *Chem. Mater.* **2005**, *17*, 953–961.

[34] Y. J. Han, J. T. Watson, G. D. Stucky, A. Butler, *J. Mol. Catal. B* **2002**, *17*, 1–8.

[35] S. B. Hartono, S. Z. Qiao, J. Liu, K. Jack, B. P. Ladewig, Z. Hao, G. Q. M. Lu, *J. Phys. Chem. C* **2010**, *114*, 8353–8362.

[36] D. I. Fried, F. J. Brieler, M. Fröba, *ChemCatChem* **2013**, *5*, 862–884.

[37] A. Dewaele, B. Van Berlo, J. Dijkmans, P. A. Jacobs, B. F. Sels, *Catal. Sci. Technol.* **2016**, *6*, 2580–2597.

[38] S. Jana, B. Dutta, R. Bera, S. Koner, *Inorg. Chem.* **2008**, *47*, 5512–5520.

[39] H. Takahashi, B. Li, T. Sasaki, C. Miyazaki, T. Kajino, S. Inagaki, *Chem. Mater.* **2000**, *12*, 3301–3305.

[40] J. M. Thomas, R. Raja, *J. Organomet. Chem.* **2004**, *689*, 4110–4124.

[41] K. Möller, T. Bein, *Chem. Mater.* **2017**, *29*, 371–388.

[42] T. I. Janjua, Y. Cao, C. Yu, A. Popat, *Nat. Rev. Mater.* **2021**, *6*, 1072–1074.

[43] C. von Baeckmann, A. Riva, P. Guggenberger, H. Kählig, S. W. Han, D. Inan, G. Del Favero, D. Berry, F. Kleitz, *Adv. Mater. Interfaces* **2022**, *9*, 2102558.

[44] C. von Baeckmann, H. Kählig, M. Lindén, F. Kleitz, *J. Colloid Interface Sci.* **2021**, *589*, 453–461.

[45] A. Popat, B. P. Ross, J. Liu, S. Jambhrunkar, F. Kleitz, S. Z. Qiao, *Angew. Chem. Int. Ed.* **2012**, *51*, 12486–12489.

[46] Q. Ye, Y. S. Zhang, *Nano TransMed* **2022**, *1*, 9130006.

[47] Q. Ni, X. Chen, *Nano TransMed* **2022**, *1*, e9130011.

[48] S. H. Wu, H. P. Lin, *Chem. Soc. Rev.* **2013**, *42*, 3862–3875.

[49] F. Tang, L. Li, D. Chen, *Adv. Mater.* **2012**, *24*, 1504–1534.

[50] E. Yamamoto, K. Kuroda, *Bull. Chem. Soc. Jpn.* **2016**, *89*, 501–539.

[51] Y. Xia, H. Zhao, S. Liu, T. Zhang, *RSC Adv.* **2014**, *4*, 2807–2812.

[52] A. Fetyan, I. Derr, M. K. Kayarkatte, J. Langner, D. Bernsmeier, R. Kraehnert, C. Roth, *ChemElectroChem* **2015**, *2*, 2055–2060.

[53] M. Inagaki, Y. Yang, F. Kang, *Adv. Mater.* **2012**, *24*, 2547–2566.

[54] S. Agarwal, J. H. Wendorff, A. Greiner, *Polymer* **2008**, *49*, 5603–5621.

[55] Y. N. Wu, F. Li, Y. Wu, W. Jia, P. Hannam, J. Qiao, G. Li, *Colloid Polym. Sci.* **2011**, *289*, 1253–1260.

[56] M. Thommes, K. Kaneko, A. V. Neimark, J. P. Olivier, F. Rodriguez-Reinoso, J. Rouquerol, K. S. W. Sing, *Pure Appl. Chem.* **2015**, *87*, 1051–1069.

[57] J. Jang, B. G. Hyun, S. Ji, E. Cho, B. W. An, W. H. Cheong, J. U. Park, *NPG Asia Mater.* **2017**, *9*, 1–10.

[58] S. Sohrabnezhad, A. Jafarzadeh, A. Pourahmad, *Mater. Lett.* **2018**, *212*, 16–19.

[59] S. Kim, H. Park, H. Choi, *Microporous Mesoporous Mater.* **2019**, *281*, 23–31.

[60] Y. Zhao, H. Wang, X. Lu, X. Li, Y. Yang, C. Wang, *Mater. Lett.* **2008**, *62*, 143–146.

[61] M. A. Elsherief, R. E. Morsi, M. Shabaan, H. Salem, S. Abdel Dayeem, M. Z. Elsabee, *Sep. Sci. Technol.* **2020**, *55*, 35–46.

[62] A. Jafarzadeh, S. Sohrabnezhad, M. A. Zanjanchi, M. Arvand, *Microporous Mesoporous Mater.* **2016**, *236*, 109–119.

[63] Y. Li, J. Zhu, H. Cheng, G. Li, H. Cho, M. Jiang, Q. Gao, X. Zhang, *Adv. Mater. Technol.* **2021**, *6*, 1–29.

[64] J. Xue, T. Wu, Y. Dai, Y. Xia, *Chem. Rev.* **2019**, *119*, 5298–5415.

[65] C. Ding, M. Breunig, J. Timm, R. Marschall, J. Senker, S. Agarwal, *Adv. Funct. Mater.* **2021**, *31*, 2106507.

[66] M. Möller, N. Tarabanko, C. Wessel, R. Ellinghaus, H. Over, B. M. Smarsly, *RSC Adv.* **2018**, *8*, 132–144.

[67] J. P. Gallas, J. M. Goupil, A. Vimont, J. C. Lavalley, B. Gil, J. P. Gilson, O. Miserque, *Langmuir* **2009**, *25*, 5825–5834.

[68] J. B. Peri, *J. Phys. Chem.* **1966**, *70*, 2937–2945.

[69] W. Bensch, W. Bergholz, *Semicond. Sci. Technol.* **1990**, *5*, 421–428.

[70] W. S. Warner, B. J. Tenge, J. M. Hungerford, D. E. Honigs, *Anal. Biochem.* **1989**, *176*, 137–149.

[71] A. Fidalgo, L. M. Ilharco, *Chem. A Eur. J.* **2004**, *10*, 392–398.

[72] D. Macina, A. Opioła, M. Rutkowska, S. Basąg, Z. Piwowarska, M. Michalik, L. Chmielarz, *Mater. Chem. Phys.* **2017**, *187*, 60–71.

[73] M. Ide, M. El-Roz, E. De Canck, A. Vicente, T. Planckaert, T. Bogaerts, I. Van Driessche, F. Lynen, V. Van Speybroeck, F. Thybault-Starzyk, P. van der Voort, *Phys. Chem. Chem. Phys.* **2013**, *15*, 642–650.

[74] S. V. Fridrikh, J. H. Yu, M. P. Brenner, G. C. Rutledge, *Phys. Rev. Lett.* **2003**, *90*, 4.

[75] P. L. Dhepe, M. Ohashi, S. Inagaki, M. Ichikawa, A. Fukuoka, *Catal. Lett.* **2005**, *102*, 163–169.

[76] S. Van De Vyver, L. Peng, J. Geboers, H. Schepers, F. De Clippel, C. J. Gommes, B. Goderis, P. A. Jacobs, B. F. Sels, *Green Chem.* **2010**, *12*, 1560–1563.

[77] S. Hamoudi, S. Royer, S. Kaliaguine, *Microporous Mesoporous Mater.* **2004**, *71*, 17–25.

[78] J. C. Manayil, C. V. M. Inocencio, A. F. Lee, K. Wilson, *Green Chem.* **2016**, *18*, 1387–1394.

[79] M. A. Isaacs, N. Robinson, B. Barbero, L. J. Durndell, J. C. Manayil, C. M. A. Parlett, C. D'Agostino, K. Wilson, A. F. Lee, *J. Mater. Chem. A* **2019**, *7*, 11814–11825.

[80] P. Choudhary, A. Sen, A. Kumar, S. Dhingra, C. M. Nagaraja, V. Krishnan, *Mater. Chem. Front.* **2021**, *5*, 6265–6278.

[81] K. Wilson, J. H. Clark, *Pure Appl. Chem.* **2000**, *72*, 1313–1319.

[82] G. Mohammadi Ziarani, N. Lashgari, A. Badiei, *J. Mol. Catal. A* **2015**, *397*, 166–191.

[83] H. Chaudhuri, S. Dash, A. Sarkar, *Ind. Eng. Chem. Res.* **2017**, *56*, 2943–2957.

[84] J. C. Mc Keen, Y. S. Yan, M. E. Davis, *Chem. Mater.* **2008**, *20*, 3791–3793.

[85] R. Marschall, J. Rathousky, M. Wark, *Chem. Mater.* **2007**, *19*, 6401–6407.

[86] S. Fujita, A. Koiwai, M. Kawasumi, S. Inagaki, *Chem. Mater.* **2013**, *25*, 1584–1591.

[87] J. Timm, R. Marschall, *Adv. Sustainable Syst.* **2018**, *2*, 1700170.

[88] J. C. Manayil, A. Osatiashtiani, A. Mendoza, C. M. A. Parlett, M. A. Isaacs, L. J. Durndell, C. Michailof, E. Heracleous, A. Lappas, A. F. Lee, K. Wilson, *ChemSusChem* **2017**, *10*, 3506–3511.

[89] J. J. Senkevich, C. J. Mitchell, G. R. Yang, T. M. Lu, *Langmuir* **2002**, *18*, 1587–1594.

[90] N. Zhang, B. Hu, *Anal. Chim. Acta* **2012**, *723*, 54–60.